



# One-dimensional magnetism and Rashba-like effects in zigzag bismuth nanoribbons

Ivan I. Naumov and Pratibha Dev <sup>\*</sup>

*Department of Physics and Astronomy, Howard University, 2355 6th Street, NW, Washington, D.C. 20059, USA*

 (Received 17 March 2022; revised 13 January 2023; accepted 15 February 2023; published 22 February 2023)

Discoveries of low-dimensional quantum materials have renewed interest in some of the fundamental phenomena, such as magnetism and Rashba-type spin orbit coupling. In particular, exploring these phenomena by themselves and/or in combination within one-dimensional (1D) systems is of interest for fields as disparate as spintronics and biology. For example, a better understanding of Rashba-type spin orbit coupling in 1D systems may be used to explain spin-selective electron transport in long helical molecules. In this paper, using first principle calculations, we show that each edge of a zigzag nanoribbon composed of a bismuth (Bi) bilayer is a truly 1D structure that naturally combines both 1D magnetism and Rashba-type spin orbit coupling in a single system. In particular, we study the combined effects of exchange and spin-orbit coupling in nanoribbons that are: (i) ideal freestanding, (ii) placed on a hexagonal boron nitride substrate, and (iii) decorated with N atoms. The edges of the Bi zigzag NRs can display ferromagnetic, antiferromagnetic, or noncollinear ordering, resulting in a broken quantum spin Hall state. The interplay of Rashba and exchange effects in different magnetic phases can result in different spin-dependent transport regimes.

DOI: [10.1103/PhysRevMaterials.7.026204](https://doi.org/10.1103/PhysRevMaterials.7.026204)

## I. INTRODUCTION

The Rashba effect refers to the spin-splitting in electronic bands due to spin-orbit coupling (SOC) that appears in the case of broken structural inversion symmetry in a crystal (due to the presence of a surface or an interface) [1,2]. The discovery of topological insulators has reinvigorated interest in the Rashba effect, with its potential to advance the field of spintronics, wherein Rashba-type SOC plays a key role in the generation and manipulation of spin currents [3]. Although the Rashba effect is normally associated with 2D systems (surfaces, thin films, layered structures), it has also been experimentally realized in 1D systems, such as gold (Au) chains on the vicinal Si(111) and Si(557) surfaces [4,5], platinum nanowires on a Si(110) surface [6], lead NRs on a Si(553) surface [7], Bi zigzag chains on an InAs(110)-(2×1) surface [8], on the edges of Bi island on a Si(111) surface [9]. New and interesting physical aspects emerge when 1D Rashba systems are subjected to an external magnetic field. If, for example, a 1D system has an electronic spectrum that consists of two spin-resolved parabolic bands (shifted relative to each other in  $k$  space), then applying an external magnetic field perpendicular to the intrinsic Rashba spin-orbit field opens a gap at the crossing point of the bands. As a result the system can be transferred into a helical liquid state, provided that the Fermi level is within the gap. Such a helical liquid state was experimentally realized in the GaAs/AlGaAs quantum wire, where a quantized conductance with opposite spins propagating in opposite directions was clearly observed [10]. Similar physical arguments explain why electrons of certain spin can traverse the helix-shaped molecules in biological

systems more easily in one direction than in the other [11]. In addition, the 1D Rashba system in a helical liquid state is a key ingredient for producing Majorana fermion bound states [12–15].

As noted by Takayama *et al.* [9], the quantum wires (nanowires) grown on semiconductor surfaces, or systems such as the Au chains on vicinal Si surfaces, are only quasi-1D and not true 1D Rashba systems. In all wires of this sort, structural inversion asymmetry (SIA) and corresponding Rashba spin-orbit coupling stem either from the underlying substrate or from the asymmetry between the opposite edges, and are not associated with single edges [16]. In contrast, the edges of a 2D topological insulator can be viewed as truly 1D Rashba systems due to the existence of topological edge states. Among the 2D topological insulators, the most known and studied is the Bi (111) bilayer, which exhibits giant spin splitting due to the fact that Bi is a heavy element with a large spin-orbit coupling. It has been suggested that applying a magnetic field or adding magnetic impurities to the bilayer will break the time-reversal symmetry and therefore can lead to new physical properties like dissipationless spin transport [9].

There are good reasons, however, to think that collective magnetism can exist in Bi structures without any external magnetic fields and any foreign magnetic impurities. Indeed, the recent discovery of ferromagnetic-like anomalous Hall effect in bismuth crystals suggests that magnetism in the system can be induced due to the presence of surfaces and grain boundaries [17]. This is consistent with the first-principles calculations [18] showing that the surface magnetization in Bi thin films due to the unsaturated Bi atoms with dangling bonds. In addition, Jin *et al.* [19] showed that (ferro)magnetism in Bi bilayers can be induced upon adsorption of the nitrogen (N) atoms on one side and

<sup>\*</sup>pratibha.dev@howard.edu

hydrogen atoms on the other side of the bilayer. Although the edges of Bi (111) nanoribbons are 1D systems, unlike the 3D and 2D Bi structures that were considered in other works [17–19], one can expect that Bi nanoribbons can also display magnetism due to similar reasons. According to the first-principles calculations for free-standing bismuth NRs [20], such a magnetism does exist at the perfect (ideal) zigzag edges, when the atoms are constrained to their bulk positions. The magnetism is induced due to unpaired electrons in the dangling bonds of the edge atoms (one electron/edge atom). However, when allowed to relax or undergo reconstruction, these edges become nonmagnetic (NM) due to the pairing of electrons in dangling bonds at the NR edges [20,21]. Although such a relaxation/reconstruction occurs in free-standing NRs, it can be inhibited when the Bi bilayers are strained and/or placed on a substrate due to various substrate effects, including the substrate friction [22,23]. We demonstrate that this is indeed the case when the Bi (111) zigzag NRs are put, for example, on a hexagonal boron nitride (hBN) monolayer. In this case, the NRs retain their geometry and magnetic order. Even stronger magnetism appears when the zigzag edges are decorated with N atoms.

Although we demonstrate two scenarios under which the Bi nanoribbons display collective magnetism, the main purpose of this paper is to use a Bi nanoribbon as a prototype structure to explore interesting physics emerging from the combined Rashba and exchange interactions in 1D systems. In Bi (111) NRs, these effects act *locally* at the opposite edges and manifest themselves via the  $\pm k$  asymmetry, an opening of a band gap (or pseudogap), spin textures with a net magnetic moment, along with the other features of the edge band structure. Such effects are most easily understood in free-standing, as-created (ideal) NRs, in which various properties are not modulated due to different sources of perturbations such as defects, adatoms, strain, and/or substrates. Hence, we first study the combined “Rashba + exchange effects” in isolation within the aforementioned as-created NRs, while eliminating other sources of perturbation. In these 1D magnetic Rashba systems, we show that the tuning of electronic chemical potential results in different regimes of spin-dependent transport. This is of interest to the field of spintronics and has not been discussed yet in the context of 1D Rashba systems. We then demonstrate practical scenarios under which magnetism at the edges can be retained by either placing NRs on the hBN substrate or by decorating it with N atoms.

## II. METHODS

We used density functional theory to study effects of Rashba SOC in combination with magnetism within three structures—Bi (111) zigzag NRs with open edges, NRs placed on the hBN substrate and NRs decorated with N atoms. These spin-resolved *ab initio* calculations were carried out by using the projector-augmented wave method [24] as implemented in the Vienna *ab-initio* simulation package (VASP) [25]. We adopted the PBE generalized gradient approximation (GGA) to describe the exchange-correlation potential [26]. In all calculations, spin-orbit coupling (SOC) was taken into account. The kinetic energy cutoff was set to 400 eV. Bi (111) zigzag NRs were created such that they were of finite width in the

$y$  direction and of infinite length in the  $x$  direction, with a supercell containing 32 Bi atoms for the freestanding NRs. As periodic boundary conditions were used, we added a vacuum gap of 25 Å in both the  $y$  and  $z$  directions to ensure negligible interaction with the images. A  $24 \times 1 \times 1$  Monkhorst-Pack  $k$ -point grid was used for the Brillouin zone sampling of the supercells. To calculate the edge energy (per length)  $\epsilon_{\text{edge}}$  in free-standing Bi (111) NRs with different edge structures, we cut the NR of interest into two equal parts along the central vertical plane in order to produce two more edges of a given type, one for each half. Then the edge energy  $\epsilon_{\text{edge}}$  was calculated according to the formula

$$E_{\text{NR}} = 2E_{\text{half}} + \epsilon_{\text{edge}}2L, \quad (1)$$

where  $E_{\text{NR}}$  is the total energy of the NRs,  $E_{\text{half}}$  is the energy of a half of the NRs, and  $L$  is the lattice parameter along the NRs. We believe that such an approach is more accurate than the standard one based on the reference to the bulk energy (per atom) because as defined above, both  $E_{\text{NR}}$  and  $E_{\text{half}}$  are calculated keeping the same supercell lattice parameters and  $k$ -point grid. Since the Klein edge structure dimerizes, to calculate its formation energy we used a  $2 \times 1$  supercell containing 64 and 32 Bi atoms for the total NR and its half, correspondingly.

We also considered two scenarios—presence of substrates and adsorption of N atoms—in which the Bi NRs display a magnetic ground state (even after relaxation). To simulate the Bi/hBN heterostructure, we used the  $(1 \times 1)$  Bi on  $(\sqrt{3} \times \sqrt{3})$  hBN commensurate structure to create the supercell, which consisted of 24 Bi atoms and a total of 96 substrate atoms (i.e., B and N atoms). Although initially commensurate, in the process of relaxation the simulated heterostructures became incommensurate in the  $y$  direction (i.e., along the direction of NR’s finite width), while the commensurability along the infinite  $x$  direction was retained. For the N-decorated Bi NRs, the zigzag edges decorated with N atoms were simulated as Klein (or “bearded”) edges, in which each N atom is attached to each edge Bi atom.

## III. RESULTS

### A. Competing edge structures of free-standing Bi bilayers

Here, we consider the relative stability of the zigzag edge-derived structures in the freestanding Bi bilayers, which previously have been identified as the most stable ones [20,21] (Fig. 1). According to Ref. [21], the Bi (111) zigzag nanoribbons favor the shear distorted edge (SE), which, however, is only slightly lower in energy (by 0.7 meV per edge atom) than the relaxed edge (RE). On the other hand, according to Ref. [20], the lowest energy structure is the one that undergoes a  $2 \times 1$  reconstruction, which can be viewed as a dimerized Klein edge (DKE). Thus, the question that naturally arises is: “What is the most stable edge structure of Bi bilayers?” Our calculations summarized in Table I show that out of the three edge terminations, DKE has the lowest formation energy. At the same time, RE and SE are almost degenerate in energy, in agreement with Ref. [21]. Surprisingly, the difference between the formation energies of DKE and RE terminations (18.1 meV per edge atom) is twenty times smaller than that predicted by Peng *et al.* [20]. This is a significant

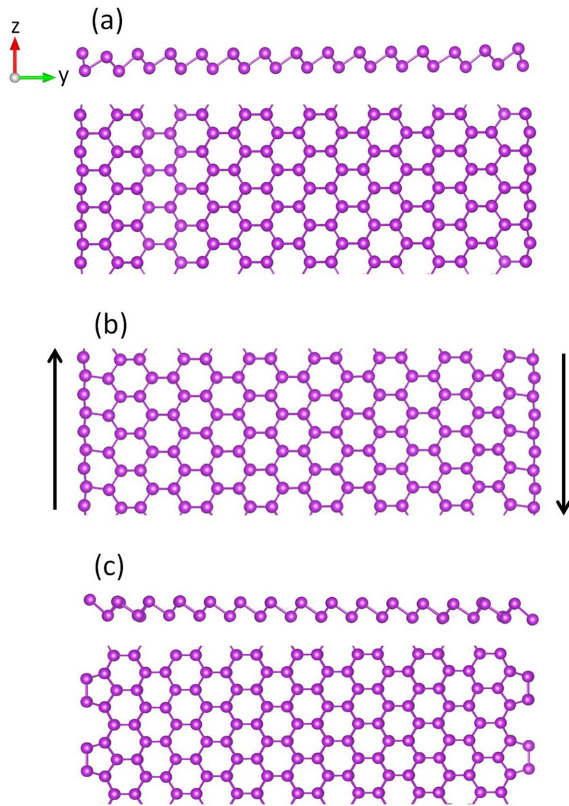


FIG. 1. (a) Side and top views of the Bi (111) NRs with the zigzag relaxed edges (REs). (b) The top view of the structure with the shear distorted edges (SEs). The black vertical arrows indicate the shear distortions. (c) The side and top views of the edge structure with the dimerized Klein edges (DKEs).

discrepancy in results, which can be attributed to the authors [20] not accounting for the SOC when determining relative structural stability. Indeed, as shown by Jeong *et al.* [21], the presence of SOC greatly affects the stability of different edge structures since the existence of topologically protected gapless edge states tends to inhibit Peierls-like distortions and  $2 \times 1$  reconstructions. Hence, our result showing a small difference between the formation energies of DKE and RE in Bi bilayers is more accurate. This is also consistent with the experimental observations [9,20,27,28]. The edges with a zigzag geometry, which we call RE in this paper, have been experimentally observed at the boundaries of single Bi-bilayer islands that form on Bi (111) surfaces of bulk crystals and/or thin films [that, in turn, are grown on a Si(111) or NbSe<sub>2</sub> substrate] [9,20,27,28]. Typically such islands appear

TABLE I. Formation energies (in meV per edge atom) for different edge structures of Bi zigzag NRs. Presented are both absolute values and relative to DKE.

Edge structure	Absolute values	Relative to DKE
RE	513.1	18.1
SE	512.4	17.4
DKE	495.0	0

in the shape of truncated triangles with alternating longer and shorter edges, with both of the edge terminations propagating along the zigzag orientations [20,27,28]. In Ref. [27], the longer (shorter) edges were named *type A* (*type B*) edges. The shorter *type B* edges, which form on the thin films, have been identified as the reconstructed DKEs [20,28], while the *type A* edges have been identified as the zigzag type (i.e., as RE) [27]. Since the *type A* (RE) edges are longer, one expects that in experiment, they are energetically more favorable or at least comparable to the DKEs, in contrast to the prediction by Peng *et al.* [20]. Hence, our calculation, which account for SOC, correctly show that RE and DKE terminations are comparable in energy. In fact, since Bi-bilayer islands in experiments were placed on substrates, it is clear that the substrates with trigonal or hexagonal symmetries tend to favor the RE structure over the DKE structure. Thus, in many practical situations the zigzag edge structure of the Bi NRs will be preserved. This is exactly what we find when we place the Bi NRs on the hBN substrate (to be discussed in detail later). It should be added that all three edge structures—RE, SE, and DKE—are nonmagnetic and display a quantum spin Hall (QSH) state, in which the edge bands (both topological and trivial) connect the bulk valence and conduction bands continuously.

### B. “Rashba + exchange” effects at perfect zigzag edges

In order to study “Rashba + exchange” effects in a true 1D structure, we first consider an ideal as-created Bi (111) zigzag NRs. In these NRs, we fix the atomic positions to those in an infinite 2D Bi bilayer with the equilibrium in-plane lattice parameter of 4.340 Å. For this as-created zigzag nanoribbons, we found three stable spin configuration, depending on different initializations of the atomic magnetic moments. The NM solution corresponds to a QSH state and is the one reported in literature for Bi-NRs studied under different situations [20,29–34]. The other two solutions for the as-created (ideal) NRs are magnetic. To date these magnetic solutions had not been considered in literature. In analogy with graphene NRs [35], we call them antiferromagnetic (AFM) and ferromagnetic (FM). Both of the magnetic structures are lower in energy than the paramagnetic structure (by  $\sim 17$  meV per edge atom). Figure 2(a) shows the band structure of the NM nanoribbon (QSH state). The edge bands are plotted in green and orange colors, while the black color is used for the bulk states. The spectrum is gapless because the edge bands connect the valence and conduction bulk bands at  $\Gamma$  and meet each other at the  $X$  point, the time-reversal invariant momentum (TRIM). The double degeneracy of the edge bands comes from the fact that there are two equivalent edges. The degenerate states from the opposite edges have opposite spins as can be seen by comparing the edge states in panel (b) with (d) and those in panel (c) with (e) within Fig. 2. Also note that the states on each edge are spin-split, with the upper and lower bands in Figs. 2(b)–2(e) tending to have opposite spins at a given  $k$ , especially near the  $\Gamma$  point. Thus, the edge states show spin splitting due to the Rashba effect. This Rashba effect is *local* in the sense that it is associated with the in-plane potential gradient at each edge. The system, however, possesses inversion symmetry  $I$ , which is *global*, as well as time-reversal symmetry  $T$ . The



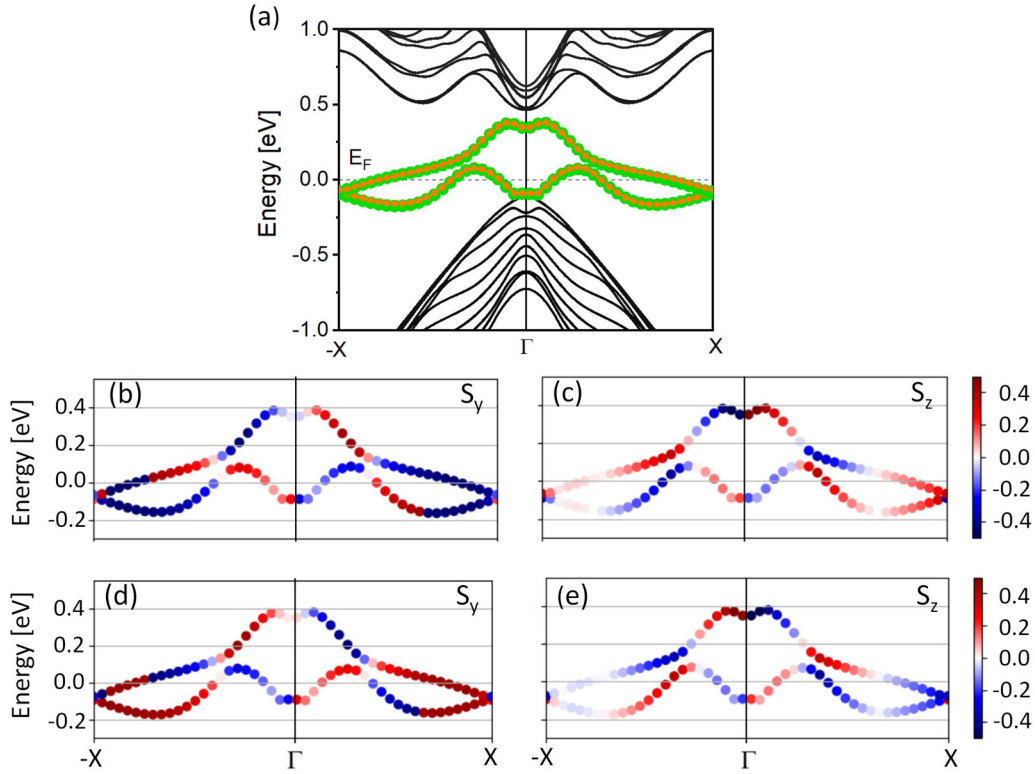


FIG. 2. Band structures of the nonmagnetic (NM) Bi (111) zigzag bilayer NR. (a) The edge bands localized on the left and right edges of the NRs are indicated by the green and orange circles, respectively. The bulk states are represented by the black curves. The edge states from the opposite sides are degenerate. Note that the gap between the edge bands and the bulk conduction bands is due to the finite width of the considered NR, which contains 16 zigzag chains. This gap should ultimately close for wider NRs, according to bulk-surface correspondence in 2D topological insulators. [(b)–(e)] Spin-resolved band structures for the edge bands localized on the left [(b),(c)] and right [(d),(e)] sides. The panels (b) and (d) correspond to the  $\pm S_y$ , while panels (c) and (e) to  $\pm S_z$  spin projections; the  $\pm S_x$  projections being small. Colors code the expectation values of the spin projections.

combination  $IT$  ensures double degeneracy for arbitrary wave vector  $\mathbf{k}$ :  $\epsilon(\mathbf{k}, \uparrow) = \epsilon(\mathbf{k}, \downarrow)$ .

In the NM state, the spin polarization  $\mathbf{S}$  of the spin-split topological surface states rotates in the  $y$ – $z$  plane in a helical manner as one traverses the Brillouin zone along the  $\mathbf{k}$  vector (parallel to the  $x$  axis) as can be seen in Figs. 2(b)–2(e). The character of rotation is very similar to that reported in Refs. [30,31]. In contrast to the typical 2D Rashba systems where the  $z$ -component of  $\mathbf{S}$  is zero, here this component is large, especially near  $\Gamma$  and midway between the  $\Gamma$  and  $X$  points. This difference between 2D and 1D Rashba systems can be understood by considering the nonrelativistic Hamiltonian operator of the spin-orbit coupling,

$$\mathcal{H}_{SO} = \frac{\hbar^2}{2m^2c^2} (\nabla V \times \mathbf{p}) \cdot \boldsymbol{\sigma}, \quad (2)$$

where  $m$  and  $\mathbf{p}$  are the mass and momentum of the electron,  $c$  is the velocity of light,  $\nabla V$  is the gradient of the potential, and  $\boldsymbol{\sigma}$  is the Pauli matrix vector. For the 1D systems being considered here, this formula can be rewritten as

$$\mathcal{H}_{SO} = \frac{\hbar^2}{2m^2c^2} (\nabla V_\rho \times \mathbf{k}_\parallel) \cdot \boldsymbol{\sigma}, \quad (3)$$

where  $\nabla V_\rho$  is the gradient of the potential perpendicular to the periodic direction ( $x$ ) of the nanoribbon,  $\mathbf{k}_\parallel$  is the momentum along the NR. In the NRs, the gradient  $\nabla V_\rho$  not only has an

out-of-plane component (which is the only component in 2D systems) but also an in-plane component due to the existence of the edges. As a result, the momentum  $\mathbf{k}_\parallel$  couples not only with the Pauli matrices  $\sigma_x$  and  $\sigma_y$ , but also with  $\sigma_z$ .

Along with the NM solution, we also obtained two magnetic solutions corresponding to AFM and FM spin alignments. The distributions of magnetization along the  $x$ ,  $y$ , and  $z$  directions in these magnetic phases are shown in Fig. 3. It turns out that in the case of the AFM phase, only the  $M_y$  and  $M_z$  components of the total magnetic moment  $\mathbf{M}$  at each edge are nonzero, with the  $M_z$  component being the dominant one ( $\sim 0.3 \mu_B$ ). These nonzero  $y$  and  $z$  components are ordered antiferromagnetically between the edges, hence the label “AFM”. In fact, there are *two* equivalent AFM states and *two* equivalent FM states; they are symmetry related and can be obtained from each other by reversing all magnetic moments. In the FM case, all the spin components at the two edges are aligned with each other. In contrast to the AFM case, here the total magnetic moment on the edges  $\mathbf{M}$  is noticeably larger in magnitude ( $\sim 1.1 \mu_B$ ), and lies in the  $x$ – $z$  plane, with a very small absolute value for  $M_y$ . As seen in the band structures [Figs. 4(a) and 4(b)] for AFM configurations, the fourfold degeneracy at the  $X$  point is lifted, and a gap  $\Delta E_{\text{ex}}$  of about 0.5 eV appears between two doubly-degenerate levels. This splitting in the energy bands is due to the exchange interaction. The edge bands are asymmetric with respect to the

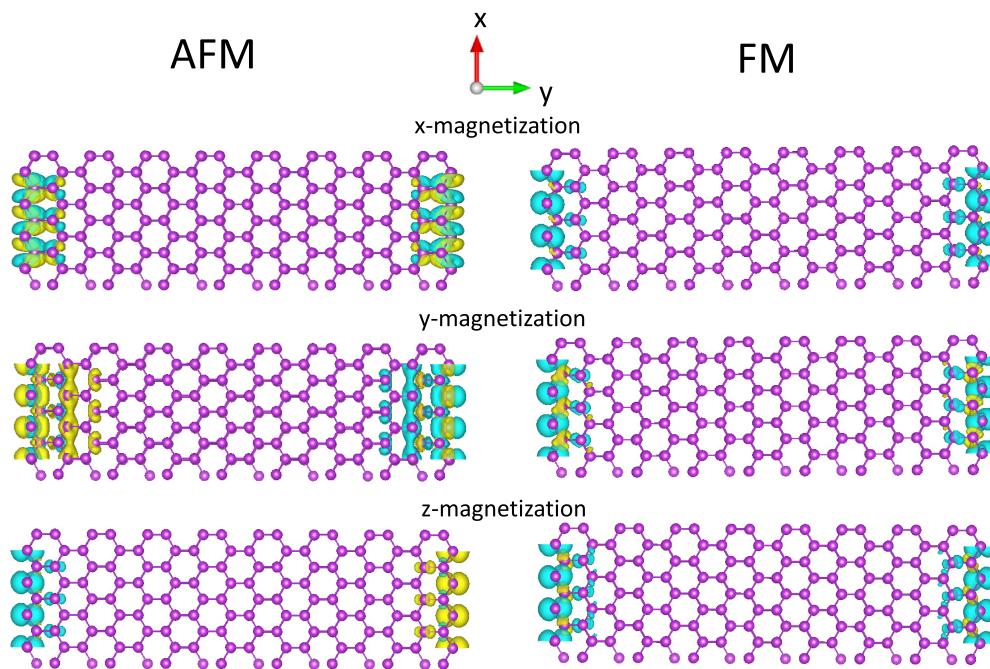


FIG. 3. Spin densities of the NR with the open edges corresponding to AFM (left panel) and FM (right panel) solutions. Blue (yellow) color indicates the negative (positive) isovalues in the isosurface plots.

origin ( $k = 0$ ) because the system is no longer invariant under both  $I$  and  $T$  symmetries if they are considered separately. In addition, as noted earlier, there are two equivalent solutions for the AFM case. For one solution, the maximum of the edge band in orange, for example, is shifted from  $\Gamma$  to the right [Fig. 4(a)], but for the other solution to the left [Fig. 4(b)]. In either case, though both  $I$  and  $T$  are broken, their combination  $IT$  is respected. Hence, just like in the case of NM solution, the bands are doubly degenerate since  $I$  and  $T$  both transform  $k$  to its inverse  $-\mathbf{k}$  [36–38]. Moreover, since  $I$  also inverts the left and right edges of the NR, the double degeneracy can

be written as  $\epsilon(\mathbf{k}, R \uparrow) = \epsilon(\mathbf{k}, L \downarrow)$ , where the labels  $L$  and  $R$  indicate the left and right edges [compare orange and green curves in Figs. 4(a) and 4(b)].

Similar to the AFM solution, for the FM case the fourfold degeneracy at the X point is also lifted due to the exchange interaction [Fig. 5(a)]. However, unlike the AFM solution, the edge bands between  $\Gamma$  and X are nondegenerate. This is owing to the fact that in the FM case, although the inversion symmetry,  $I$ , is preserved, the simultaneous symmetry,  $IT$ , is broken due to the broken time-reversal symmetry [36–38]. The presence of  $I$ , makes the band structure symmetric relative to  $\Gamma$ :

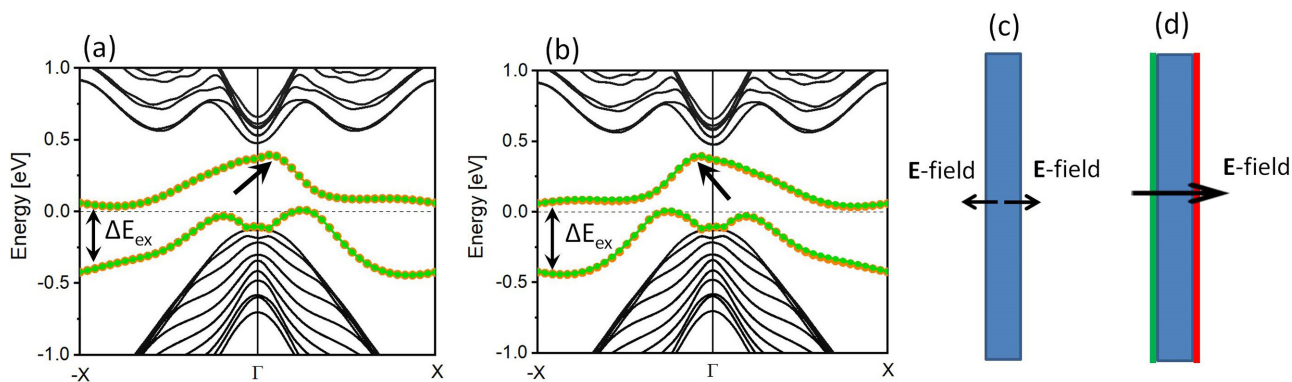


FIG. 4. [(a),(b)] Band structures of the magnetic Bi (111) zigzag bilayer NR for the AFM stable self-consistent spin configurations. The edge bands localized on the left and right edges of the NRs are indicated by the orange and green circles, respectively. The bulk states are represented by the black curves. Two different band structures (a) and (b) correspond to two equivalent AFM solutions with opposite spin moments. Similar to the NM case, for the AFM structure, the edge states from the opposite sides are degenerate. To emphasize this, the orange circles in panels (a) and (b) are made larger to stand out. The oblique black arrows indicate the shift of the bands along the  $k$  axis relative to those in the nonmagnetic phase [see Fig. 2]. (c) Schematic diagram showing Rashba effect in Bi zigzag NRs acting locally at each edge, where the potential gradients or electric fields develop. This is in contrast with the ordinary 1D systems, where such fields are usually associated with the nonequivalent edges (d).

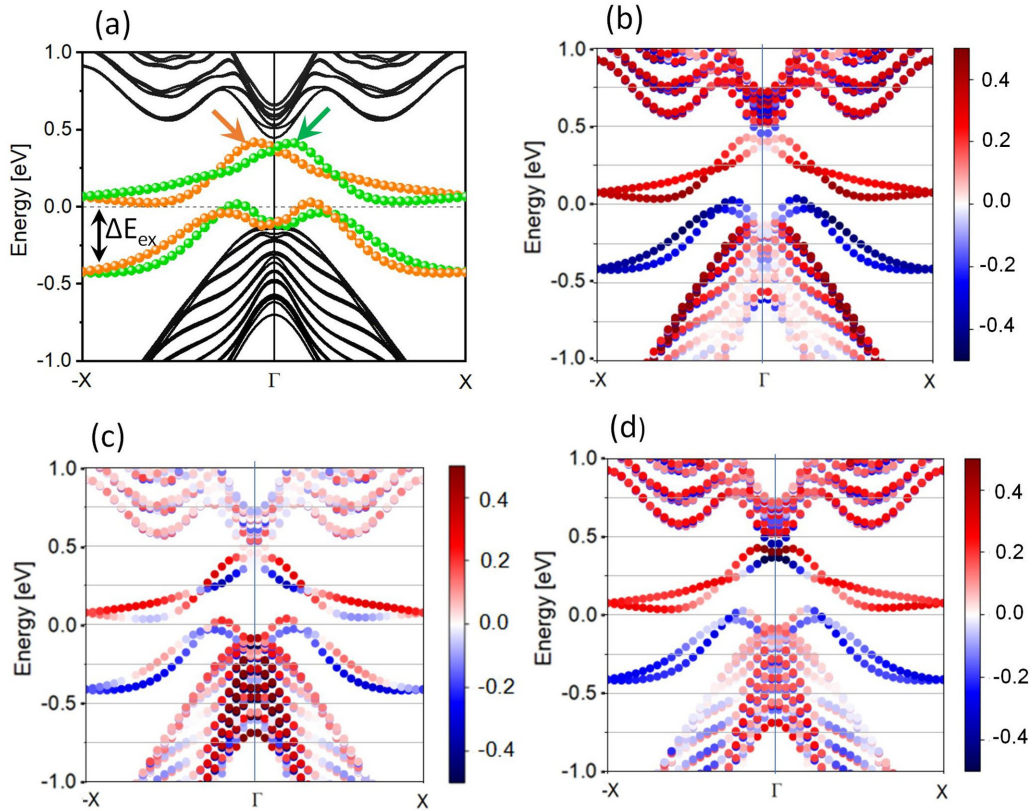


FIG. 5. Band structure for the Bi (111) zigzag bilayer NR with the FM configuration, without (a) and with [(b),(c),(d)] spin projections. In the panel (a) the edge bands localized on the left and right edges of the NRs are indicated by the orange and green circles, respectively. The panels (b), (c), and (d) correspond to the  $\pm S_x$ ,  $\pm S_y$ , and  $\pm S_z$  spin projections, respectively. Colors code the expectation values of the spin projections.

$\epsilon(\mathbf{k}, R \uparrow) = \epsilon(-\mathbf{k}, L \uparrow)$  [compare orange and green curves in Fig. 5(a)]. These curves cross each other at the inversion-invariant momenta,  $\Gamma$ ,  $-X$ ,  $X$ , since for them  $-\mathbf{k} = \mathbf{k}$ . As the ferromagnetic order develops, it shifts the bands localized on a particular edge along or against the  $\mathbf{k}$  vector, so that, for example,  $\epsilon(\mathbf{k}, R \uparrow) \neq \epsilon(-\mathbf{k}, R \uparrow)$ . This is similar to what was observed in the AFM case.

The shift of the edge bands relative to  $\Gamma$  in the AFM and FM phases is a result of the interplay between the Rashba and exchange effects [39]. In the AFM case, the magnetic moment at each edge is directed mostly along the  $z$  (or  $-z$ ) direction, i.e., *perpendicular* to the  $\mathbf{k}$  vector. In such a situation, the bands should shift along the  $\mathbf{k}$  vector [39], and this is indeed the case. The bands with the opposite spins at the opposite edges shift in the *same* direction. This fact actually means that the Rashba effect in our systems operates *locally* at each edge, where the potential gradients and electric fields develop. This is shown in the schematic diagram in Fig. 4(c), and it is in contrast to what takes place in ordinary trivial 1D systems, where the Rashba SOC is usually induced by SIA associated with the nonequivalent edges [see Fig. 4(d)].

In Fig. 5, along with the edge-resolved band structure [Fig. 5(a)], we also plot spin-resolved band structures in the FM phase [Figs. 5(b)–5(d)]. These band structures augment the real-space information provided by Fig. 3 for the FM phase and help to understand the corresponding distributions of magnetization and total magnetic moments. Both the left

and right edge valence bands can be seen in Figs. 5(b) and 5(d) to have mostly negative spin components  $S_x$  and  $S_z$  when the  $\mathbf{k}$  traverses from  $-X$  to  $X$ . Hence, at both edges, the  $x$  and  $z$  components of total magnetic moment  $\mathbf{M}$  are negative and are relatively large in magnitudes. On the other hand, the same bands tend to switch their  $S_y$  component upon the reversing the  $\mathbf{k}$  vector [Fig. 5(c)]. This explains why the  $y$  component of the total magnetic moment at both edges, although negative, is relatively small in magnitude. The detailed information provided in edge- and spin-resolved band structures [Figs. 5(a)–5(d)], along with the real-space spin-density plots [Fig. 3] point towards a possibility of different transport regimes in Bi NRs (see the discussion in Sec. III E).

### C. “Rashba + exchange” in Bi nanoribbons placed on the hBN monolayer

We now consider an experimentally-relevant situation when a Bi NR is placed on a substrate, such as an hBN monolayer. The corresponding heterostructure can be described by a  $(1 \times 1)$  Bi on  $(\sqrt{3} \times \sqrt{3})$  hBN moiré supercell, with a very small lattice mismatch of an only about 0.2–0.3%. Although there are infinite possibilities corresponding to the horizontal shifts of the Bi bilayer relative to the hBN monolayer, we considered three types of starting alignments (i.e., stacking orders before relaxation) between the two components—Bi and hBN—of the composite. These three stacking orders



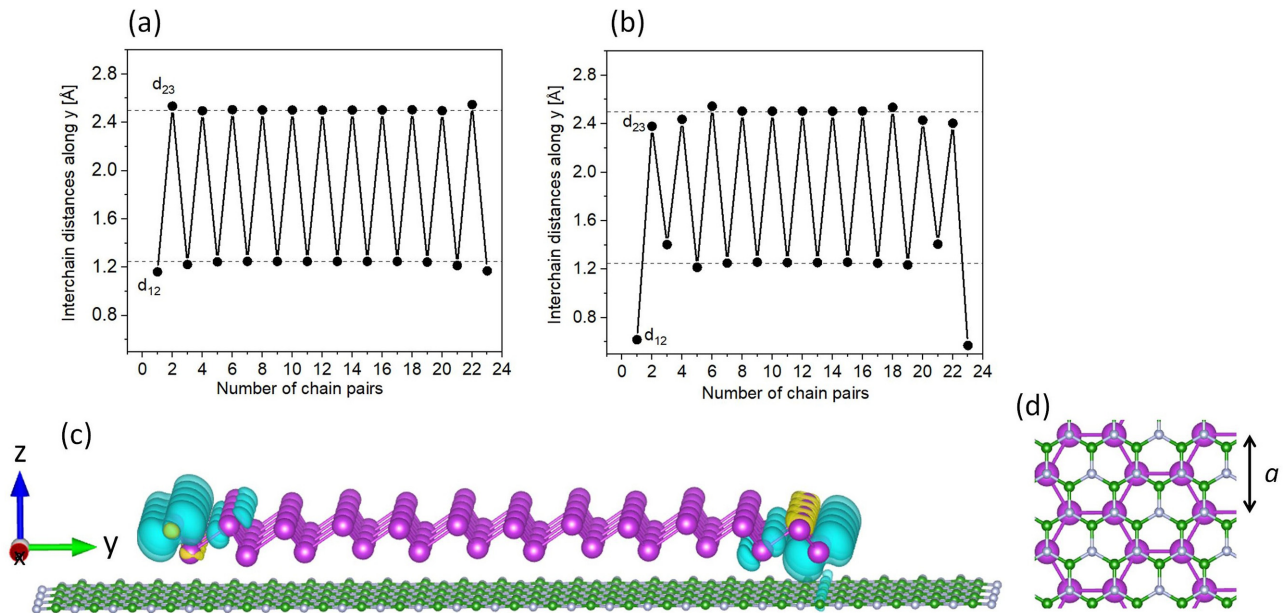


FIG. 6. Separations between the neighboring chains of Bi atoms, straight and parallel to  $x$ , in the  $y$  direction in the relaxed Bi/hBN(N) heterostructures obtained without (a) and with (b) the inclusion of SOC at  $a = 4.340$  Å. The pairs of chains are counted in the direction from the left edge to the right. The horizontal dash lines are guides for the eye showing the distances in the middle of the NRs. (c) Spin density (its dominant  $y$  component) for the Bi/hBN(N) heterostructure with the FM configuration and corresponding to panel (a). Blue (yellow) color indicates the negative (positive) isovalues in the isosurface plots. The total magnetic moments of the heterostructure is  $[0.00, -0.60, 0.46] \mu_B$ . (d) Top view of the heterostructure. The grey circles indicate N atoms and green—B atoms.

correspond to all Bi atoms of the bilayer, before structural relaxation, directly on top of: (i) the B atoms in hBN [referred to as Bi/hBN(B)], (b) N atoms [referred to as Bi/hBN(N)], and centers of hBN hexagons [referred to as Bi/hBN(H)]. When all atoms are allowed to relax, we find that only the outmost Bi atoms and their nearest neighbors change their positions noticeably. The relative stability of the different stacking orders depends on whether or not SOC is taken into account. Without the inclusion SOC, Bi/hBN(B) is the lowest energy structure, while the lowest energy structure is found to be Bi/hBN(N) once SOC is included in the calculations.

Interestingly, all the relaxed Bi/hBN structures found without the inclusion of SOC in calculations exhibit both FM and AFM magnetic ordering. However, the magnetism disappears in going to the optimized structures obtained with SOC. In order to understand why the heterostructure relaxed with and without the SOC effects display different magnetic properties, we compared the respective structures for relaxed Bi/hBN(N) composite [obtained for  $a = 4.340$  Å, lattice constant for an isolated bilayer sheet]. Figures 6(a) and 6(b) show how far the neighboring chains of Bi atoms, straight and parallel to  $x$ , are separated from each other in the  $y$  direction (*i.e.*, across the NRs). One can clearly see that the SOC effects lead to more pronounced edge relaxations and thus, to the quenching of the magnetism at this particular  $a$ .

Our explanation above for the loss of magnetism when SOC is included in the calculations, also indicates that increasing the distances between dangling bonds at the edges can be a way to retain magnetism in the composite. We find that this is indeed the case and in spite of SOC, Bi bilayer placed on hBN retains its magnetism if it is stretched

by a small amount (by 2% or more). It should be added that the slight straining of the free standing Bi-bilayer NRs does not result in magnetism. Hence, we find that we need a combination of both strain (whether present intentionally or unintentionally) and substrate effects to obtain magnetic structures.

We now concentrate on an unstrained ferromagnetic Bi/hBN(N) heterostructure, obtained without the inclusion of SOC [corresponds to Fig. 6(a)]—it exhibits similar band structure as the ones stretched and relaxed with the inclusion of SOC. This heterostructure has a total magnetic moments of  $[0.00, -0.60, 0.46] \mu_B$ , and its distribution of magnetization along the  $y$  direction is presented in Fig. 6(c). The corresponding band structure resembles that for the FM phase in free-standing systems (*cf.* Figs. 7 and 5). Now, however, the (two) edge bands localized at the left (right) side of the NR cross each other approximately at one/half of the way from  $-X$  to  $\Gamma$  (from  $\Gamma$  to  $X$ ). The other differences come from the fact that now the inversion symmetry  $I$  is broken: The opposite edges of the NRs become inequivalent because one edge terminating in the upper Bi atoms within the buckled Bi bilayer is now closer to the vacuum, whereas the opposite edge, which terminates with the lower Bi atoms, is closer to the substrate layer. As a result, the band structure is no longer symmetric relative to the origin, resulting in  $\epsilon(\mathbf{k}, R \uparrow) \neq \epsilon(-\mathbf{k}, L \uparrow)$ . Moreover, the pairs of edge bands from the opposite edges do not cross any longer at the  $X$  and  $\Gamma$  points. The crossing point of the two lower bands shifts from  $-X$  to the right. At the  $\Gamma$  point, small energy gaps of  $\sim 17$  and  $27$  meV open up for the pair of edge-derived valence and conduction bands, respectively. These energy gaps can be understood as gaps between the bonding and antibonding bands due to hybridization

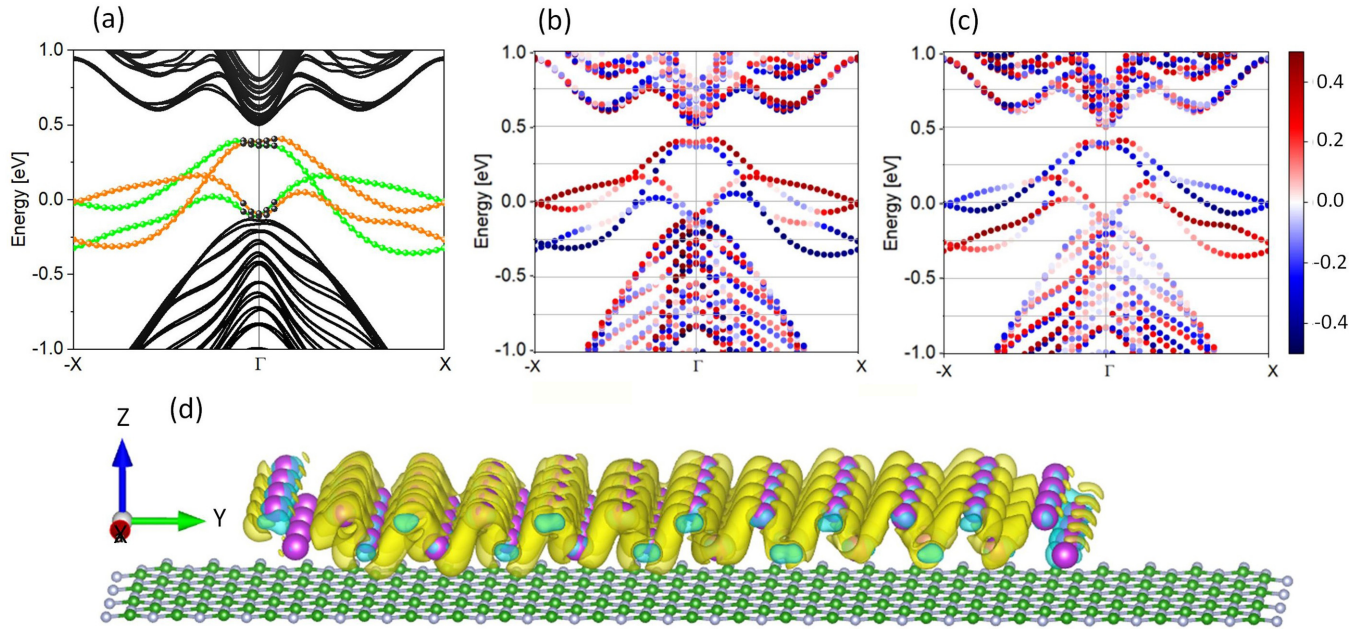


FIG. 7. Band structure for the Bi/hBN(N) heterostructure with the FM configuration, without (a) and with [(b),(c)] spin projections. In the panel (a) the edge bands localized on the left and right edges of the NRs are indicated by the orange and green circles, respectively. Within the narrow  $k$  interval centered on  $\Gamma$ , where the orange and green circles are replaced by black ones, the states are not well localized and spread over the entire NR width as  $k \rightarrow \Gamma$  (see the main text). The panels (b) and (c) correspond to the  $\pm S_y$  and  $\pm S_z$  spin projections, respectively. (d) Charge density plot for the highest-energy state at the  $\Gamma$  point, which is results from hybridization between the edge states and is delocalized over the entire region between the two edges.

between the right and left edge states. Such a hybridization is especially pronounced within the narrow  $k$  interval centered around  $\Gamma$ , as shown in Fig. 7(a) by replacing orange and green circles by black ones. Within this interval, the wavefunctions are no longer localized to one of the edges as seen in Fig. 7(d), which is plot of one of these hybridized state (highest energy state) at the  $\Gamma$  point. It can be seen to be delocalized over the region spanning between the two edges.

#### D. Zigzag nanoribbons decorated with N atoms

As mentioned earlier, the magnetic structures for the as-created NRs are lower in energy than the paramagnetic solution (by  $\sim 17$  meV per edge atom) but not significantly. Therefore, we considered ways in which the magnetic structures can be stabilized to a greater extent relative to the NM solution. One possible way to achieve this is by adsorbing nonmagnetic atoms, such as nitrogen, on the edges [19,40]. To study the effect of N-atom decoration, the Bi atoms along the edges were passivated with N atoms, transforming the zigzag edges into Klein (or “bearded”) edges. Upon relaxation, the Bi-N bond was found to be  $1.97 \text{ \AA}$  with a variation of about  $\pm 0.02 \text{ \AA}$  for different stable spin configurations. As in the previous case of open edges, the self-consistent calculations yielded three stable and metastable spin configurations, which we denote as NM, FM and FM-AFM. Both of the magnetic structures are significantly lower in energy than the NM structure (by  $650$  meV per N atom), whereas the FM structure is lower than the FM-AFM structure by  $10$  meV. In the FM phase, all three components of the total magnetic moment  $\mathbf{M}$  are ferromagnetically ordered between the edges. In the case

of the FM-AFM structure, however, we obtain a noncollinear magnetic ordering. In this case, only the  $M_x$  components phase are parallel to each other, while the other two— $M_y$  and  $M_z$ —are antiparallel. In both the FM and FM-AFM phases, the  $M_x$  component is relatively small in magnitude.

In what follows, we will discuss the lowest energy solution (FM) in greater detail. Figure 8(a) shows the band structure of the nonmagnetic N-decorated nanoribbons. Figure 8(a) shows that: (i) the edge bands span the bandgap as well as connect the valence and conduction bands and (ii) there are an odd number of edge-bands crossings (at  $E_F$ ) between the  $\Gamma$  and X points. This strongly supports the presence of the QSH state in the decorated NR. Hence, we find that the edge bands, which originate from the dangling bond states, are transformed into topological surface states due to the topological nature of Bi bilayers. The introduction of ferromagnetic order changes the band structure dramatically opening up a noticeable band gap at  $E_F$  ( $\sim 0.2$  eV) and splitting the fourfold degenerate energy levels at the X point [see Fig. 8(b)] due to the exchange interaction. In addition, just as in the case of NR with open edges, although the inversion symmetry  $I$  in the FM phase is preserved,  $IT$  is broken due to the broken time-reversal symmetry. This lifts the degeneracies between  $\Gamma$  and X points. The edge bands localized at the opposite sides are shifted in the opposite directions relative to  $\Gamma$  [compare the bands in orange and green in Fig. 8(b)]. The shift, however, is noticeably smaller as compared to that for FM bare/undecorated NR despite the fact that the magnetic moment of the FM N-decorated nanoribbon is significantly larger [ $\sim 4 \mu_B$  per supercell]. This can be explained by the fact that the band shift is controlled not only by the magnitude of magnetization



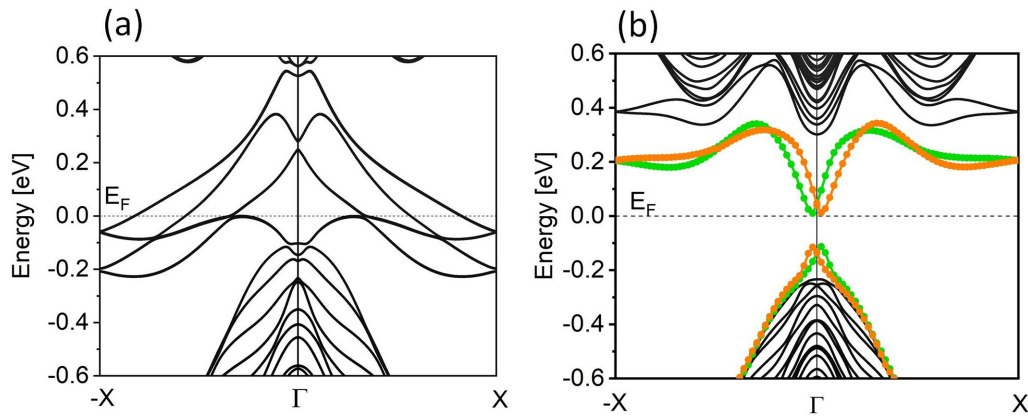


FIG. 8. Band structure for the Bi (111) zigzag bilayer NR decorated with nitrogen atoms, for the (a) NM and (b) FM states. In (b), the bands drawn with orange (green) circles are localized at the left (right) edge of the decorated NR.

and gradient of the edge potential but also by the SOC of the outmost atoms [41]. Here, the outmost atoms are nitrogen with relatively weak SOC. The calculated magnetic moment of  $\sim 4 \mu_B$  per supercell (or equivalent to  $2 \mu_B$  per N atom) is mostly contributed by the nitrogen atom's  $p_x$  and  $p_z$  orbitals, which are poorly aimed at the nearest Bi atoms and therefore, only slightly hybridized with bismuth's  $p$  orbitals (in contrast to  $p_y$ ). Figure 9 shows the distributions of magnetization in a FM nanoribbon whose net magnetic moment is  $\mathbf{M} = [-1.15, -2.22, 2.90] \mu_B$ . In magnitude, this is three times the magnetic moment calculated for the FM NR without N decoration. Small contributions to the net magnetic moment also come from the nearest and next-nearest-neighboring bismuth atoms, with moments on nearest neighboring Bi atoms antiparal-

lel and those on next-nearest neighboring Bi parallel to the moments on N atoms. The distributions of magnetization in Fig. 9 are consistent with the corresponding spin-resolved band structure shown in Fig. 10. Indeed, the spin polarized bands across the Fermi level in Fig. 10 show that the  $x$  and  $y$  components of the total magnetic moment should be negative, while the  $z$  component positive.

### E. Possible transport regimes

Our results reveal that the magnetic Rashba Bi (111) NRs can exhibit different transport regimes when doped, or subjected to an external electric field. To illustrate this, consider only the ideal zigzag NRs. If, for example, the chemical

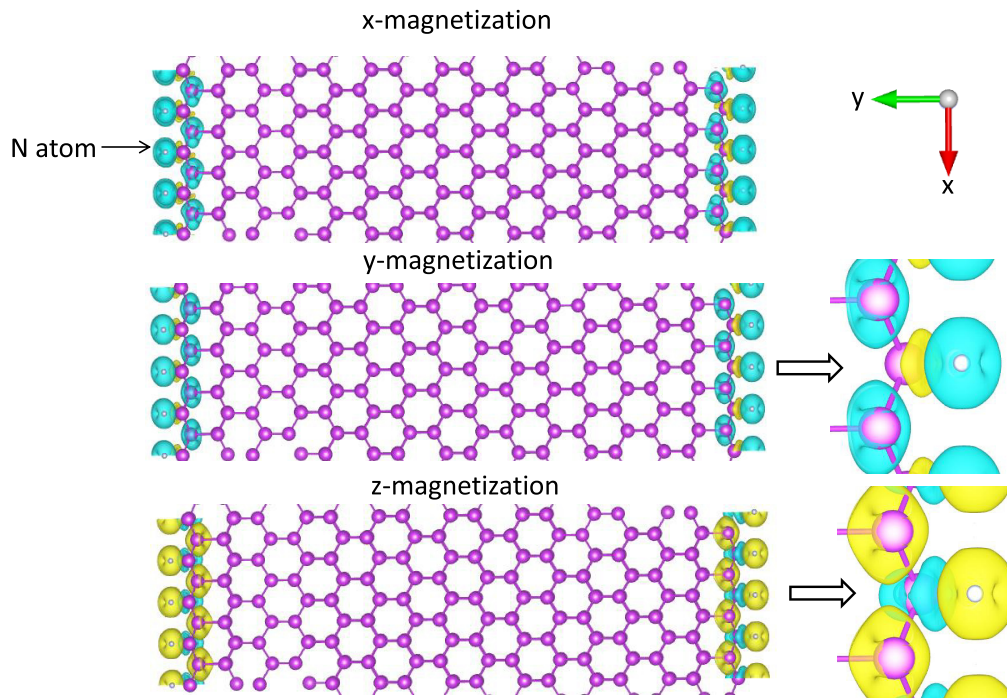


FIG. 9. Spin densities of a NR with the edges decorated with nitrogen, for a FM solution. Yellow (blue) colors in the spin density plots correspond to positive (negative) isovalues of the plotted quantity. In the cases of  $x$  and  $z$  magnetizations, an expanded view of the NR edges are shown on the right.

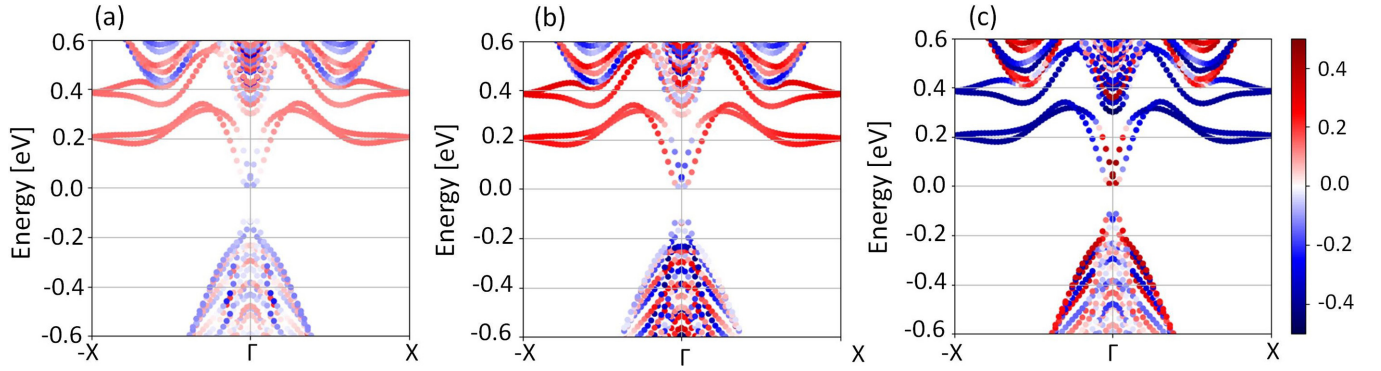


FIG. 10. Band structure for the NR decorated with nitrogen atoms with FM spin configuration, showing spin projections. The panels (a), (b), and (c) correspond to the  $\pm S_x$ ,  $\pm S_y$ , and  $\pm S_z$  spin projections, respectively. Colors code the expectation values of the spin projections.

potential  $\mu$  is tuned to be located within the conduction band (say, at  $\sim 0.2$  eV) in Fig. 5, then the FM phase is forced into a half-metallic state, resulting in metallic behavior only for the spin-up electrons (more precisely, with the positive  $S_x$  and  $S_z$  spin projections). This corresponds to a completely spin polarized electric current, which changes in magnitude if its direction is reversed or in going to the opposite edge, as shown in Fig. 11. Under a similar doping, the AFM phase becomes metallic for the spin-down channel on the left edge but for the spin up channel on the right edge. The magnitude of the current again changes if its direction is reversed (see Fig. 11). New and interesting transport regimes can be achieved by applying an in-plane electric field across the NRs. If, for instance, such a field is applied to the AFM state, then half-metallicity can be achieved, similar to the case of graphene nanoribbons as discussed in Ref. [42]. This also means that the magnetic properties of the NRs can be controlled by external electric fields.

When heavily  $n$  doped, the FM Bi (111) NRs with N decoration will behave similar to their FM counterparts with open edges, as far as their edge transport regime is concerned. This can be seen from the spin-resolved band structure shown in Fig. 10. On the other hand, for a smaller extent of  $n$  doping, the edge states will counterpropagate along the same edge with opposite spins, thus resembling QSH state.

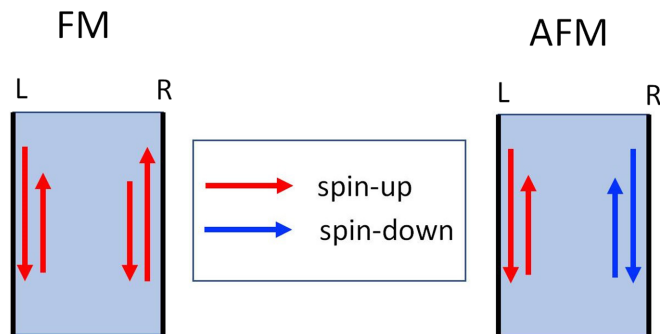


FIG. 11. Schematic of transport in the FM and AFM Bi zigzag NRs under  $n$  doping. The edge states carrying opposite spins are denoted by red and blue.

#### IV. DISCUSSION AND SUMMARY

In this paper, we demonstrated that the Rashba and exchange effects act locally at each edge of the Bi zigzag NRs due to the topological edge states. To better understand and appreciate this result, it is instructive to compare our results with those obtained for the 1D Rashba magnetic systems of conventional type, such as graphene zigzag nanoribbons (ZGNR) in the presence of foreign magnetic elements. As shown in Refs. [43,44], ZGNR become magnetic by adsorbing, in particular, magnetic gadolinium (Gd) atoms. It was found that when the Gd atoms are adsorbed right at the center of the nanoribbon, which preserves the spatial inversion symmetry, the Gd-ZGNR does not show any Rashba spin splitting and the band structure does not shift as the magnetization direction is changed. In contrast, in our FM phases, reversing the magnetization also reverses the shift of the bands on each particular edge, with the green curves in Figs. 5(a) and 8(b) transforming into orange ones and vice versa, leaving the band structure effectively unchanged. Further, when the Gd atoms in a Gd-ZGNR are adsorbed on the asymmetric sites and break the spatial inversion symmetry, the Rashba effect comes into play and the band structure exhibits opposite horizontal shifts for the opposite magnetizations (along  $[001]$  and  $[00\bar{1}]$ ). The shifted bands stem from the hybridized Gd- $5d$  and C- $p_z$  orbitals and are not confined to the edges, as contrasted to Bi (111) NRs, where such bands are localized at the edges.

This different manifestation of the Rashba effect in Gd-ZGNRs and Bi (111) NRs (decorated or not) can be explained in the following way. In ZGNRs with the Gd atom adsorbed at asymmetric sites, the Rashba-effect is associated with the transverse electric field, which is caused by the asymmetry of the NRs as a *whole* [as in Fig. 4(d)]. On the other hand, in the Bi (111) counterparts, the Rashba effect is associated with the local electric fields that are generated at the border between the edges and vacuum [as in Fig. 4(c)]. Formally, the Rashba-type effect in Gd-ZGNRs should be considered as Dresselhaus effect. This is because in the Gd-ZGNRs with the asymmetric placements of Gd atoms, the inversion symmetry of the supercell is broken in the same way as the inversion center in the crystal. In contrast, the Rashba effect in Bi (111) nanoribbons results from the edge electric fields, which are analogous to the electric field across the “surface-vacuum” interface, or between two different layers in 2D Rashba systems.

In summary, our study reveals interesting interplay between exchange and Rashba effects in Bi (111) bilayer zigzag NRs, with ideal edges, on a BN substrate and decorated with N atoms. In order to understand this interplay of exchange and Rashba effects, these effects were first studied a free-standing ideal zigzag NRs, eliminating all other sources of perturbations to the NR properties. Since the ideal zigzag NRs have a center of symmetry and a mirror plane, it makes it easier to interpret the results. We found that the ideal NRs can exist not only in a paramagnetic (or quantum spin Hall) state but also in two magnetic states (FM and AFM) that are lower in energy. These magnetic states are analogous to the ones predicted for zigzag-type graphene NRs [35]. The presence of magnetism significantly modifies the band structure inherent to QSH state, leading to the  $\pm k$  asymmetry and opening up a band gap (or pseudogap). The results for zigzag NRs are then used as a scaffolding to interpret more complex and experimentally-relevant systems—Bi/hBN heterostructures and Bi nanoribbons decorated with N atoms. We find that the basic properties of the freestanding as-created Bi bilayer are retained in these more complicated systems, which can be realized in experiments. When doped, the

magnetic 1D Rashba systems demonstrate unusual, asymmetric spin-dependent transport properties. Thus, our results open the possibility for new applications of 1D systems in electronics. This is especially favorable in view of the fact that recently the templated growth of 1D nanomaterials using multiwalled carbon nanotubes have been extended to ribbon-like morphologies. In particular, ultranarrow TaS<sub>2</sub> NRs (with widths below 3 nm, and lengths greater than 10 nm) have been successfully synthesized [45].

#### ACKNOWLEDGMENTS

This work was supported by the W. M. Keck Foundation and the NSF Grant No. DMR-1752840. We acknowledge the computational support provided by the Extreme Science and Engineering Discovery Environment (XSEDE) under Project No. PHY180014, which is supported by National Science Foundation Grant No. ACI-1548562. We also acknowledge VESTA 3 software for three-dimensional visualization of crystals and volumetric data and the use of *PyProcar* to create figures with spin textures [46].

- 
- [1] F. T. Vas'ko, Spin splitting in the spectrum of two-dimensional electrons due to the surface potential, *Pis'ma Zh. Eksp. Teor. Fiz.* **30**, 574 (1979).
- [2] Y. A. Bychkov and E. I. Rashba, Properties of a 2D electron gas with lifted spectral degeneracy, *Pis'ma Zh. Eksp. Teor. Fiz.* **39**, 66 (1984).
- [3] A. Manchon, H. C. Koo, J. Nitta, S. M. Frolov, and R. A. Duine, New perspectives for Rashba spin-orbit coupling, *Nat. Mater.* **14**, 871 (2015).
- [4] I. Barke, F. Zheng, T. K. Rugheimer, and F. J. Himpsel, Experimental Evidence for Spin-Split Bands in a One-Dimensional Chain Structure, *Phys. Rev. Lett.* **97**, 226405 (2006).
- [5] T. Okuda, K. Miyamoto, Y. Takeichi, H. Miyahara, M. Ogawa, A. Harasawa, A. Kimura, I. Matsuda, A. Kakizaki, T. Shishidou, and T. Oguchi, Large out-of-plane spin polarization in a spin-splitting one-dimensional metallic surface state on Si(557)-Au, *Phys. Rev. B* **82**, 161410(R) (2010).
- [6] J. Park, S. W. Jung, M.-C. Jung, H. Yamane, N. Kosugi, and H. W. Yeom, Self-Assembled Nanowires with Giant Rashba Split Bands, *Phys. Rev. Lett.* **110**, 036801 (2013).
- [7] M. Kociuszyński, M. Krawiec, R. Zdyb, and M. Jałochowski, Purely one-dimensional bands with a giant spin-orbit splitting: Pb nanoribbons on Si(553) surface, *Sci. Rep.* **7**, 46215 (2017).
- [8] T. Nakamura, Y. Ohtsubo, Y. Yamashita, S.-i. Ideta, K. Tanaka, K. Yaji, A. Harasawa, S. Shin, F. Komori, R. Yukawa, K. Horiba, H. Kumigashira, and S.-i. Kimura, Giant Rashba splitting of quasi-one-dimensional surface states on Bi/InAs(110)-(2×1), *Phys. Rev. B* **98**, 075431 (2018).
- [9] A. Takayama, T. Sato, S. Souma, T. Oguchi, and T. Takahashi, One-Dimensional Edge States with Giant Spin Splitting in a Bismuth Thin Film, *Phys. Rev. Lett.* **114**, 066402 (2015).
- [10] C. H. L. Quay, T. L. Hughes, J. A. Sulpizio, L. N. Pfeiffer, K. W. Baldwin, K. W. West, D. Goldhaber-Gordon, and R. de Picciotto, Observation of a one-dimensional spin-orbit gap in a quantum wire, *Nat. Phys.* **6**, 336 (2010).
- [11] K. Michaeli and R. Naaman, Origin of spin-dependent tunneling through chiral molecules, *J. Phys. Chem. C* **123**, 17043 (2019).
- [12] M. Z. Hasan and C. L. Kane, Topological insulators, *Rev. Mod. Phys.* **82**, 3045 (2010).
- [13] X.-L. Qi and S.-C. Zhang, Topological insulators and superconductors, *Rev. Mod. Phys.* **83**, 1057 (2011).
- [14] R. M. Lutchyn, J. D. Sau, and S. Das Sarma, Majorana Fermions and a Topological Phase Transition in Semiconductor-Superconductor Heterostructures, *Phys. Rev. Lett.* **105**, 077001 (2010).
- [15] Y. Oreg, G. Refael, and F. von Oppen, Helical Liquids and Majorana Bound States in Quantum Wires, *Phys. Rev. Lett.* **105**, 177002 (2010).
- [16] A. G. Syromyatnikov, S. V. Kolesnikov, A. M. Saletsky, and A. L. Klavsyuk, Formation and properties of metallic atomic chains and wires, *Phys. Usp.* **64**, 671 (2021).
- [17] B. C. Camargo, P. Gierowski, A. Alafrodov, I. N. Demchenko, M. Sawicki, K. Gas, and Y. Kopelevich, Anomalous Hall effect in bismuth, *J. Magn. Magn. Mater.* **525**, 167581 (2021).
- [18] I. I. Naumov and P. Dev, Quantum materials interfaces: Graphene/bismuth (111) heterostructures, *Phys. Rev. Res.* **2**, 023157 (2020).
- [19] K.-H. Jin and S.-H. Jhi, Quantum anomalous Hall and quantum spin-Hall phases in flattened Bi and Sb bilayers, *Sci. Rep.* **5**, 8426 (2015).
- [20] L. Peng, J.-J. Xian, P. T. A. Rubio, S.-C. Zhang, W. Zhang, and Y.-S. Fu, Visualizing topological edge states of single and double bilayer Bi supported, on multibilayer Bi(111) films, *Phys. Rev. B* **98**, 245108 (2018).
- [21] S.-M. Jeong, S. Yi, H.-J. Kim, G. Bihlmayer, and J.-H. Cho, Competing edge structures of Sb and Bi bilayers generated by



- trivial and nontrivial band topologies, *Phys. Rev. B* **98**, 075402 (2018).
- [22] P. Manchanda, P. Kumar, and P. Dev, Thickness dependence of hydrogen-induced phase transition in  $\text{MoTe}_2$ , *Phys. Rev. B* **101**, 144104 (2020).
- [23] P. Manchanda, P. Kumar, and P. Dev, Defect-induced  $4p$ -magnetism in layered platinum diselenide, *Phys. Rev. B* **103**, 144403 (2021).
- [24] G. Kresse and D. Joubert, From ultrasoft pseudopotentials to the projector augmented-wave method, *Phys. Rev. B* **59**, 1758 (1999).
- [25] G. Kresse and J. Furthmüller, Efficient iterative schemes for *ab initio* total-energy calculations using a plane-wave basis set, *Phys. Rev. B* **54**, 11169 (1996).
- [26] J. P. Perdew, K. Burke, and M. Ernzerhof, Generalized Gradient Approximation Made Simple, *Phys. Rev. Lett.* **77**, 3865 (1996).
- [27] I. K. Drozdov, A. Alexandradinata, S. Jeon, S. Nadj-Perge, H. Ji, R. J. Cava, B. A. Bernevig, and A. Yazdani, One-dimensional topological edge states of bismuth bilayers, *Nat. Phys.* **10**, 664 (2014).
- [28] N. Kawakami, C.-L. Lin, M. Kawai, R. Arafune, and N. Takagi, One-dimensional edge state of Bi thin film grown on  $\text{Si}(111)$ , *Appl. Phys. Lett.* **107**, 031602 (2015).
- [29] H. Kotaka, F. Ishii, M. Saito, T. Nagao, and S. Yaginuma, Edge states of Bi nanoribbons on Bi substrates: First-principles density functional study, *Jpn. J. Appl. Phys.* **51**, 025201 (2012).
- [30] F. Yang, L. Miao, Z. F. Wang, M.-Y. Yao, F. Zhu, Y. R. Song, M.-X. Wang, J.-P. Xu, A. V. Fedorov, Z. Sun, G. B. Zhang, C. Liu, F. Liu, D. Qian, C. L. Gao, and J.-F. Jia, Spatial and Energy Distribution of Topological Edge States in Single  $\text{Bi}(111)$  Bilayer, *Phys. Rev. Lett.* **109**, 016801 (2012).
- [31] D. Wang, L. Chen, H. Liu, and X. Wang, Electronic structures and topological properties of  $\text{Bi}(111)$  ultrathin films, *J. Phys. Soc. Jpn.* **82**, 094712 (2013).
- [32] Z. F. Wang, L. Chen, and F. Liu, Tuning topological edge states of  $\text{Bi}(111)$  bilayer film by edge adsorption, *Nano Lett.* **14**, 2879 (2014).
- [33] X. Li, H. Liu, H. Jiang, F. Wang, and J. Feng, Edge engineering of a topological  $\text{Bi}(111)$  bilayer, *Phys. Rev. B* **90**, 165412 (2014).
- [34] H. W. Yeom, K.-H. Jin, and S.-H. Jhi, Topological fate of edge states of Bi single bilayer on  $\text{Bi}(111)$ , *Phys. Rev. B* **93**, 075435 (2016).
- [35] H. Lee, Y.-W. Son, N. Park, S. Han, and J. Yu, Magnetic ordering at the edges of graphitic fragments: Magnetic tail interactions between the edge-localized states, *Phys. Rev. B* **72**, 174431 (2005).
- [36] J. P. Tang, Q. Zhou, G. Xu, and S.-C. Zhang, Dirac fermions in an antiferromagnetic, *Nat. Phys.* **12**, 1100 (2016).
- [37] L.-D. Yuan, Z. Wang, J.-W. Luo, E. I. Rashba, and A. Zunger, Giant momentum-dependent spin splitting in centrosymmetric low- $Z$  antiferromagnets, *Phys. Rev. B* **102**, 014422 (2020).
- [38] L.-D. Yuan, Z. Wang, J.-W. Luo, and A. Zunger, Prediction of low- $Z$  collinear and noncollinear antiferromagnetic compounds having momentum-dependent spin splitting even without spin-orbit coupling, *Phys. Rev. Mater.* **5**, 014409 (2021).
- [39] O. Krupin, G. Bihlmayer, K. Starke, S. Gorovikov, J. E. Prieto, K. Döbrich, S. Blügel, and G. Kaindl, Rashba effect at magnetic metal surfaces, *Phys. Rev. B* **71**, 201403(R) (2005).
- [40] K.-H. Jin and S.-H. Jhi, Effect of atomic impurities on the helical surface states of the topological insulator  $\text{Bi}_2\text{Te}_3$ , *J. Phys.: Condens. Matter* **24**, 175001 (2012).
- [41] L. Petersen and P. Hedegard, A simple tight-binding model of spin-orbit splitting of *sp*-derived surface states, *Surf. Sci.* **459**, 49 (2000).
- [42] Y.-W. Son, M. L. Cohen, and S. G. Louie, Half-metallic graphene nanoribbons, *Nature (London)* **444**, 347 (2006).
- [43] Z. Qin, G. Qin, B. Shao, and X. Zuo, Unconventional magnetic anisotropy in one-dimensional Rashba system realized by adsorbing Gd atom on zigzag graphene nanoribbons, *Nanoscale* **9**, 11657 (2017).
- [44] Z. Qin, G. Qin, B. Shao, and X. Zuo, Rashba spin splitting and perpendicular magnetic anisotropy of Gd-adsorbed zigzag graphene nanoribbon modulated by edge states under external electric fields, *Phys. Rev. B* **101**, 014451 (2020).
- [45] J. D. Cain, S. Oh, A. Azizi, S. Stonemeyer, M. Dogan, M. Thiel, P. Ercius, M. L. Cohen, and A. Zettl, Ultranarrow  $\text{TaS}_2$  nanoribbons, *Nano Lett.* **21**, 3211 (2021).
- [46] U. Herath, P. Tavadze, X. He, E. Bousquet, S. Singh, F. Muñoz, and A. H. Romero, PyProcar: A Python library for electronic structure pre/post-processing, *Comput. Phys. Commun.* **251**, 107080 (2020).